MATERIALS SCIENCE

Extraordinary tensile strength and ductility of scalable nanoporous graphene

Hamzeh Kashani[1], Yoshikazu Ito[2], Jiuhui Han[3], Pan Liu[3], Mingwei Chen[1,3]*

While the compressive strength-density scaling relationship of ultralight cellular graphene materials has been extensively investigated, high tensile strength and ductility have not been realized in the theoretically strongest carbon materials because of high flaw sensitivity under tension and weak van der Waals interplanar bonding between graphene sheets. In this study, we report that large-scale ultralight nanoporous graphene with three-dimensional bicontinuous nanoarchitecture shows orders of magnitude higher strength and elastic modulus than all reported ultralight carbon materials under both compression and tension. The high-strength nanoporous graphene also exhibits excellent tensile ductility and work hardening, which are comparable to well-designed metamaterials but until now had not been realized in ultralight cellular materials. The excellent mechanical properties of the nanoporous graphene benefit from seamless graphene sheets in the bicontinuous nanoporosity that effectively preserves the intrinsic strength of atomically thick graphene in the three-dimensional cellular nanoarchitecture.

INTRODUCTION

Lightweight and mechanically robust cellular materials are important for widespread application in ultralight structures, energy absorption, electronic devices, energy storage and conversion, biomedicine, and so on (*1*–*6*). The elastic modulus (E) and yield strength (σ) of open cellular materials can be described by the density scaling equations, $E \propto E_b\bar{\rho}^n$ and $\sigma \propto \sigma_b\bar{\rho}^m$, where $\bar{\rho}$ is the relative density and E_b and σ_b are Young's modulus and yield strength of parent solid materials, respectively (*7*–*9*). Exponents of n and m are the geometrically mechanical response of a cellular structure displaying either stretching-dominated behavior with $n = 1$ and $m = 1$ or bending-dominated behavior with $n > 2$ and $m > 1.5$ (*7*). The stretching-dominated mode is expected to provide higher strength and stiffness as indicated by the exponents because the struts of frameworks are mainly subjected to axial tension or compression in the longitudinal direction (*8*, *10*). In contrast, the bending-dominated mode has lower strength and stiffness but offers more flexibility and ductility for higher energy absorption. For ultralight materials with a density below 10 mg cm^{-3}, such as aerogels and stochastic cellular materials, the strength commonly follows a quadratic or reduced cubic density scaling law (*9*, *11*) except for recently developed ultralight microlattices with optimized geometric configurations for stretching-dominated deformation (*3*, *9*). Although the ultralight materials often have excellent mechanical properties in compression, high tensile strength and modulus are rarely realized despite increasing demands for tensile properties from a technological perspective and from a fundamental interest in understanding the mechanics of ultralight cellular materials (*4*).

In addition to the geometric effect, the strength and modulus of ultralight cellular structures are also determined by the intrinsic mechanical properties and density of parent solid materials. Graphene, mono– or few–atomic layer carbon, is the strongest and stiffest material ever known so far (*12*) and, thus, is an ideal parent material for constructing ultralight and ultrastrong cellular structures, especially for bearing tensile loading. Three-dimensional (3D) cellular graphene materials have been fabricated by using different approaches (*13*–*19*). However, all the reported graphene materials suffer from substantial degradation in strength and modulus and are limited to bear the compressive loading by following quadratic to cubic density scaling laws because of the uncontrollable porosity and weak interconnectivity between graphene sheets by van der Waals interplanar bonding (*20*, *21*). Inspired by the recent achievements of high mechanical properties from metamaterials with a hierarchical hollow tubular structure (*3*, *4*), we develop bicontinuous nanoporous graphene that is constructed by a seamless tubular graphene network by nanoporous metal–based chemical vapor deposition (CVD) to effectively use the excellent in-plane properties of graphene at a macroscopic scale. The freestanding and scalable nanoporous graphene with hierarchical nanoarchitecture has a tunable tubular diameter and wall thickness to maximize load carrier capability and shows excellent tensile and compressive properties superior to all other graphene and carbon cellular materials reported in the literature.

RESULTS

Nanoporous graphene is synthesized by a nanoporous Ni (np-Ni)–based CVD method in which dealloyed np-Ni with 3D bicontinuous open nanoporosity is used as both a nanoporous template and a catalyst for graphene growth (Fig. 1A) (*22*, *23*). After completely removing the Ni substrates and supercritical drying, centimeter-sized freestanding nanoporous graphene samples can be achieved (Fig. 1, B and C). The density of the resulting nanoporous graphene is tuned in a wide range from an ultralow value of 3 mg cm^{-3} to 70 mg cm^{-3} by tailoring graphene wall thicknesses and the pore sizes of np-Ni templates. The number of graphene layers (i.e., wall thickness) is tailored from monolayer to multilayers by controlling graphene growth time from 0.3 to 10 min. We characterized the graphene layers of the monolayer and bilayer graphene samples by 2D and G band intensity (I_{2D}/I_G) ratios and the full width at half maximum (FWHM) of the 2D bands of Raman spectra in Fig. 1E and fig. S1 (*24*). For monolayer graphene, the I_{2D}/I_G ratio is higher than 2 and the FWHM of the 2D peak is lower than 45 cm^{-1}, while the bilayer graphene has an I_{2D}/I_G ratio between 1 and 2 and an FWHM between 45 and 60 cm^{-1} (*24*–*26*). The measured intensity ratios (I_{2D}/I_G) and the FWHM of the samples

[1]Department of Materials Science and Engineering, Johns Hopkins University, Baltimore, MD 21214, USA. [2]Institute of Applied Physics, Graduate School of Pure and Applied Sciences, University of Tsukuba, Tsukuba 305-8573, Japan. [3]Advanced Institute for Materials Research, Tohoku University, Sendai 980-8577, Japan.
*Corresponding author. Email: mwchen@jhu.edu

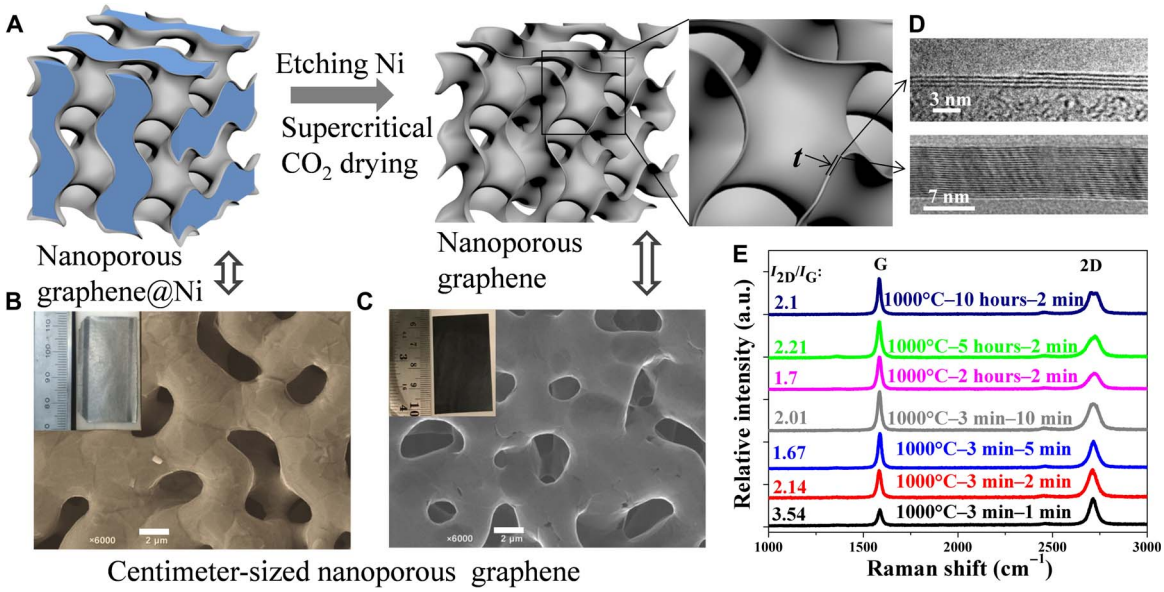

Fig. 1. Fabrication and microstructure characterization of nanoporous graphene. (**A**) Schematic illustration of CVD-grown bicontinuous nanoporous graphene and a tubular structure with atomically thick walls. (**B**) Scanning electron microscopy (SEM) image of nanoporous graphene@Ni. Inset: A centimeter-sized sample. (**C**) SEM image of freestanding nanoporous graphene after etching away Ni. Inset: A centimeter-sized sample. (**D**) High-resolution transmission electron microscopy (TEM) images showing a few-atomic-layer graphene wall in low-density nanoporous graphene grown at 1000°C for 1 min and a multilayer graphene wall in high-density nanoporous graphene grown at 1000°C for 10 min. The wall thickness of graphene tubes is tunable from monolayer, bilayer, to multilayer by changing graphene growth time from 1 to 10 min. (**E**) Raman spectra of nanoporous graphene with different np-Ni annealing times before graphene growth and CVD growth periods at 1000°C. We annealed all np-Ni substrates at 1000°C for 3 min before CVD growth of graphene at various times from 1 to 10 min to change the thickness of graphene or fixed the CVD growth time and tuned the np-Ni annealing periods from 3 min to 10 hours to change the tube/pore sizes as marked on each Raman spectrum. a.u., arbitrary units. Scale bars, 2 μm (B and C).

with different growth conditions are summarized in table S1. For multilayer graphene samples, we measured the layers by direct observations using high-resolution transmission electron microscopy (HRTEM) (Fig. 1D) and the estimation of the areal density of graphene sheets on the basis of the Brunauer-Emmett-Teller (BET) surfaces and densities. The pore sizes are designed between ~350 nm and 3 μm by controlling nanopore coarsening through changing the annealing time and temperature of np-Ni substrates (fig. S2). As usual, a larger pore size and a thinner graphene wall give rise to a lower density (table S1). Uniaxial tension experiments of dog bone–shaped samples with a gauge length of 6 mm, a width of 2 mm, and a thickness of 35 μm are conducted at a constant displacement mode with a nominal strain rate of $8.3 \times 10^{-4}\ s^{-1}$ at room temperature. The gauge dimensions are limited by the thickness of the nanoporous graphene, and the 6 mm by 2 mm gauge dimensions are in the safe range to prevent lateral and transverse buckling/wrinkling of the thin foil samples according to the ASTM E345 standard (Test Methods of Tension Testing of Metallic Foil). For comparison, we also investigated the compression properties of the samples using nanoindentation with a large 20-μm-diameter spherical indenter at a loading rate of 0.0178 mN s^{-1} (fig. S3). We noticed that the tensile properties of the nanoporous graphene samples show an obvious dependence on the CVD temperatures. With a near-identical density of ~20 mg cm^{-3}, the ultimate strength and the elastic modulus significantly increase from 234 kPa and 3.8 MPa to 432 kPa and 6.6 MPa by increasing the CVD temperature from 800° to 900°C (Fig. 2A). Raman spectra (fig. S1A) suggest that the 800°C CVD graphene is more defective with a relatively higher I_D/I_G ratio of 0.278 while the 900°C sample has excellent crystallinity with a lower I_D/I_G ratio of 0.03. Apparently, the lower defect density from higher CVD temperatures can significantly improve the tensile properties of nanoporous graphene. Thus, all the nanoporous graphene samples used in this study are grown at 900° or 1000°C and have a near-perfect crystallinity, as evidenced by ignorable defect bands (*D*) in Raman spectra (Fig. 1E and fig. S1, C and D).

Similar to other cellular materials, the strength of the nanoporous graphene intrinsically depends on the density (Fig. 2B). The sample with the highest density of 70 mg cm^{-3} in this study gives the highest tensile strength and modulus of 1.2 and 48 MPa, while the sample with the lowest density of 3 mg cm^{-3} exhibits the lowest ultimate strength and modulus of 85 kPa and 0.8 MPa, respectively. The tensile strength of nanoporous graphene is slightly higher than compression (Fig. 3A and tables S1 and S2), different from other cellular materials that usually have much lower tensile strength (*27*). The reliability of the measured mechanical properties is verified by the consistent elastic moduli of tension and compression for each sample. Besides the strength and modulus, the tensile ductility of the nanoporous graphene also shows density dependence. There is a distinct "brittle-to-ductile" transition at a density of ~20 mg cm^{-3} (Fig. 2B). The samples with a thicker wall and a density larger than 20 mg cm^{-3} only experience a linear elastic deformation before catastrophic fracture at the peak strength. In contrast, the samples with a thinner wall and a density below 20 mg cm^{-3} have large nonlinear tensile strains up to 13%, accompanied by obvious strain hardening before failure (Fig. 2B, inset), which is similar to ductile metals. The dependencies of strength and modulus on density are plotted in Fig. 3 (A and B). Both tension and compression strengths and moduli of the high-quality nanoporous graphene are obviously higher than those of cellular graphene assemblies (*11*, *17*, *18*, *28*) and metallic lattices (*29*) in the entire density range of this study (fig. S4).

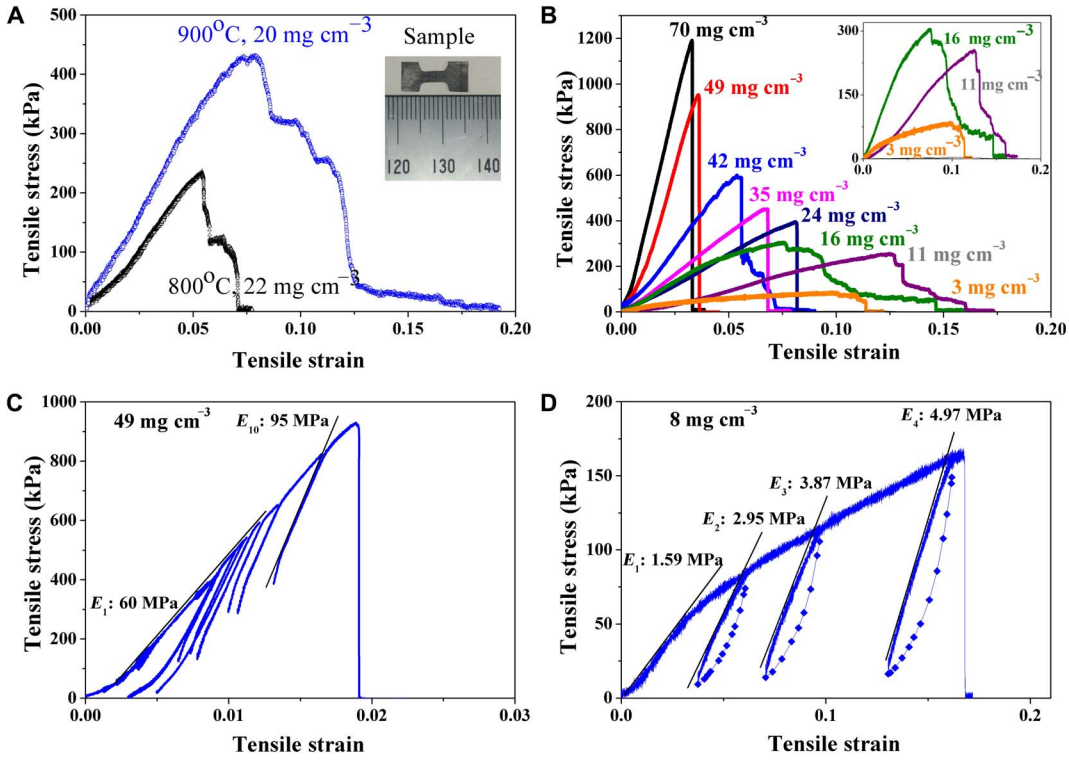

Fig. 2. Tensile stress-strain curves of nanoporous graphene. (**A**) Effect of graphene growth temperature on the tensile properties of nanoporous graphene. Inset: The dog bone–shaped tensile sample with a total length of 15 mm and a gauge length of 6 mm. (**B**) Tensile stress-strain curves of high-quality nanoporous graphene with different densities between 3 and 70 mg cm^{-3}. Inset: Tensile stress-strain curves of low-density nanoporous graphene. (**C**) Multistep loading-unloading of nanoporous graphene with a density of 49 mg cm^{-3}. Curves show obvious self-stiffening where the modulus is increased from the original value of 60 MPa to 95 MPa (50%) in the last loading before fracture. (**D**) Multistep loading-unloading of nanoporous graphene with a density of 8 mg cm^{-3}. Self-stiffening and work hardening are remarkable as the modulus is increased from 1.59 to 4.97 MPa (~300%).

Significantly, in the ultralow-density range (<10 mg cm^{-3}), the tensile strength of the nanoporous graphene surpasses the compression strength and elastic moduli of all high-strength cellular materials reported in the literature (*16*–*19*, *30*). The modulus of nanoporous graphene can be scaled with relative density $\bar{\rho}$ as $E \propto \bar{\rho}^m$, with the exponent $m = 1.6$. However, the strength cannot be scaled by a single exponent but by two exponents as $\sigma \propto \bar{\rho}^{1.5}$ in the low-density range ($\bar{\rho} <$ 20 mg cm^{-3}) and $\sigma \propto \bar{\rho}^{1.1}$ in the high-density range ($\bar{\rho} >$ 20 mg cm^{-3}), corresponding to the brittle-to-ductile transition with density and changes in deformation modes from high-density stretching-dominated deformation to low-density bending-mediated deformation. The modulus and strength exponents of the nanoporous graphene exceed the quadratic and stochastic behaviors of previously reported porous graphene assemblies, cellular graphene foams (*16*–*21*, *30*, *31*), graphene aerogel microlattices (*16*), nanocarbon lattices (*32*), tetrahedral tubular graphene (*33*), and carbon nanotube (CNT) foams (*34*, *35*). The scaling response of nanoporous graphene is superior to the expectation of traditional bending-dominated foams with power exponents of 2 and 1.5 for modulus and strength, respectively (*7*), suggesting that the bicontinuous tubular structure likely deforms in different manners, overwhelming the full bending mode under both tension and compression loading conditions. In particular, the density-dependent deformation demonstrates that the stretching-dominated tension at the high-density region offers higher strength but poor ductility while the mixed mode of stretching and bending in the low-density nanoporous graphene gives rise to both high strength and good ductility.

Cyclic tensile loading-unloading tests with various strain steps were implemented to investigate the two representative deformation/fracture modes of nanoporous graphene with densities of 49 and 8 mg cm^{-3}, which are above and below the brittle-to-ductile transition, respectively. For the sample with a density of 49 mg cm^{-3}, the initial elastic modulus is 60 MPa and gradually increases to 95 MPa (~50% increment) in the last cycle before fracture (Fig. 2C). The self-stiffening may result from the irreversible rotation and realignment of graphene tubes along the loading direction. However, the ultimate strength is close to that of the single tensile testing. From the scanning electron microscopy (SEM) images taken from the fracture surfaces, obvious buckling of graphene tubes cannot be seen in the vicinity of fracture zones (fig. S5B). The brittleness may arise from the rigidity of thick graphene walls, which leads to highly concentrated stresses at nodes for formation and fast propagation of cracks. In contrast, the low-density sample with mono– or few–atomic layer graphene demonstrates a significant strain hardening and self-stiffening. The modulus increases from the initial 1.59 MPa before the yield point to 4.97 MPa (~300% increment) right before fracture after 13% nonelastic strain, together with a considerable strength increase from the yield point of 60 kPa to the ultimate value of 165 kPa (Fig. 2D). Although the maximum tensile strain of the low-density nanoporous graphene is not as high as those of elastic materials (*13*), it is higher than or comparable to other nanoporous materials with a similar morphology (*27*) and microlattices (*4*, *36*) because of the contribution from the bending portion of the mixed deformation mode.

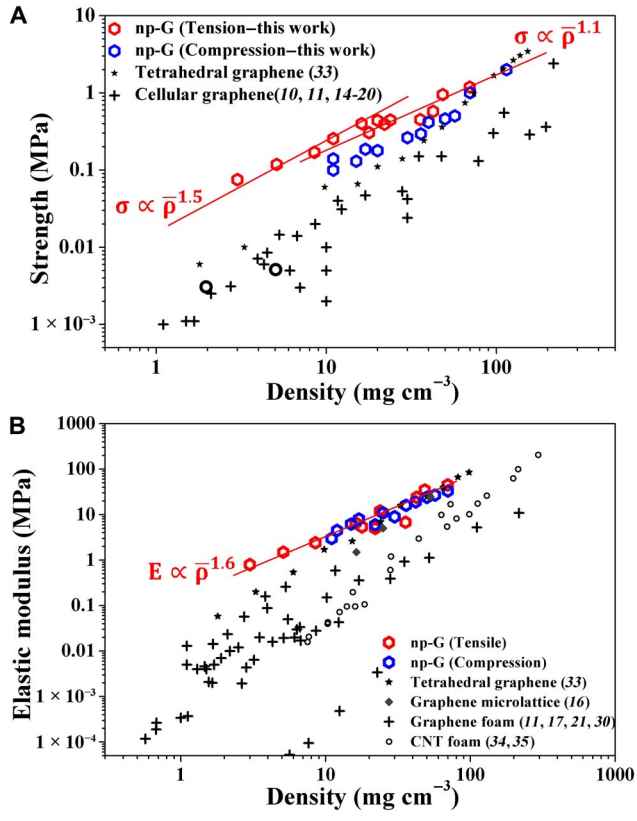

Fig. 3. Mechanical properties versus density of high-strength ultralight carbon materials. (**A**) Tensile and indentation yield strength versus density of nanoporous graphene. For comparison, the graphene and CNT-based porous materials from the literature are also plotted. The black open circles represent the tensile strength of graphene foam, which has a coarse pore size of about 100 μm, and the high aspect ratio of struts fabricated using CVD of Ni foam (*37*). (**B**) Tensile and indentation elastic modulus versus density of nanoporous graphene and other ultralight graphene and carbon materials.

DISCUSSION

To understand the deformation and failure mechanisms of the nanoporous graphene, particularly the self-stiffening and work hardening, we conducted in situ straining SEM observations. The yielding of the low-density sample results from extensive elastic shell buckling in nodes of graphene tubes, which leads to the realignment of tubular graphene toward the loading direction (fig. S6). Graphene is an anisotropic material that is extremely strong under in-plane tension but very soft and flexible when subjected to out-of-plane bending. Apparently, the gradual realignment of the atomically thin sheets along the tensile direction from the easily deformed out-of-plane (bending) mode to the strong in-plane (stretching) mode gives rise to self-stiffening and work hardening. The work hardening in the random hollow tube nanostructures is also the result of competition between realignment of hollow tubes in the loading direction and stretching fracture of tubes and depends on the density and the thickness of tube walls. Fractured hollow tubes that lack load carrier capability under tension reduce stress, whereas redirecting the tubes in the loading direction causes applied stress to increase (*37*). As manifested by smooth nonlinear stress-strain curves before fracture (Fig. 2, B and D), realignment of tubes toward the loading direction proved to be dominant in the low-density nanoporous graphene (<20 mg cm^{-3}), whereas the impeded bending/buckling in the thick-walled tubes (high-density samples) causes brittle fracture in the linear elastic region. Therefore, thin-walled tubes facilitate the bending and buckling capacity of the nodes (fig. S6, A to D). The extensive realignment of tubes toward the loading direction (fig. S6) leads to not only high self-stiffening and work hardening but also large tensile strains by bridging crack tips and delaying crack propagation (fig. S6, E and F). Visible changes in the overall thickness and width of the tensile sample cannot be seen after a large elongation of 17% (fig. S7), indicating a near-zero or even negative Poisson ratio of the nanoporous graphene. The deformation behavior of the marked graphene tubes in fig. S6 implies that the nonlinear deformation of graphene tubes is accompanied by the increase of tube length. The shell buckling and tube rotation at nodes contribute to the deformation of low-density nanoporous graphene and give rise to the high strength and ductility of the seamless interconnected tubular frameworks with an ultralow density (*3*).

In general, the coupling between growth flaws and concentrated stresses at node junctions of hollow tube frameworks is responsible for poor mechanical properties, particularly under tension (*33*, *38*). Our tubular graphene has a smooth connection at the node junctions with a morphology similar to that of the triply periodic minimal surface (TPMS) with near-zero mean curvature, which is adopted from the self-assembled nanoporous metal substrates (*39*). The TPMS architecture is expected to afford the stretch mode of deformation as the thin shells carry loads by coplanar stresses (*10*). The seamless connection at the node junctions of graphene tubes would render excellent tensile properties in terms of specific tensile strength, modulus, and ductility (figs. S4 and S8). Moreover, depending on topology and connectivity, deformation of struts in bending-dominated porous structures is modulated from fully bending (in low strut coordination at nodes) to a mixture of stretching-bending (with a coordination number higher than 4) (*40*). Apparently, the low aspect ratio and high coordination number of the graphene tubes in nanoporous graphene favor the stretching-bending behavior.

In summary, we developed ultrastrong and ductile 3D nanoporous graphene materials with ultralow densities for tensile applications. The unique bicontinuous nanoarchitecture constructed by interconnected high-quality graphene tubes offers high tensile strength and ductility, as well as an unprecedented damage tolerance at extremely low density. The high load and strain carrier capabilities of the nanoporous graphene benefit from the mixed deformation mode of stretching and bending and result in scaling relationships of $E \propto \bar{\rho}^{1.6}$ and $\sigma \propto \bar{\rho}^{1.1}$. Notably, the bicontinuous porous nanoarchitecture greatly preserves not only the excellent mechanical properties but also the 2D electronic behaviors and the large specific surface area of graphene (*22*, *23*, *41*). Therefore, the ultralight, strong, and ductile nanoporous graphene holds great promise for a wide range of structural and functional applications.

MATERIALS AND METHODS

Synthesis of nanoporous graphene

np-Ni templates with a pore size of ~10 nm were prepared by chemically dealloying $Ni_{30}Mn_{70}$ alloy sheets in 1 M $(NH_4)_2SO_4$ solution (*42*). The dealloyed np-Ni with a thickness of 35 μm was loaded into a CVD furnace as the templates of nanoporous graphene growth. Before CVD growth, the np-Ni templates were annealed at different temperatures (800°, 900°, and 1000°C) under a flowing mixed gas of 2500 standard cubic centimeters per minute (sccm) of Ar and 100 sccm of H_2 for various periods (3 min to 6 hours) to tune the pore sizes (i.e., the diameter of graphene tubes). Subsequently, nanoporous graphene samples were grown by introducing a carbon source of benzene (0.1 mbar, 99.8%,

anhydrous; Sigma-Aldrich) at a CVD temperature of 900° or 1000°C. The number of graphene layers (thickness of graphene tube walls) was tuned from monolayer, bilayers, to multilayers by altering graphene growth time (0.3 to 10 min). 3D nanoporous graphene samples were achieved by dissolving the np-Ni templates in 3 M HCl acid solution and by rinsing four times with deionized water. After the samples were rinsed several times with 2-propanol, they were immersed in 2-propanol for 1 week to completely exchange the entrapped water inside the nanoporous structure. Subsequently, the 2-propanol was exchanged with supercritical liquid CO_2 (at a flow rate of 6 ml min^{-1}) at a temperature of 70°C and at a pressure of 15 MPa for 7 hours. After the treatment, the temperature and pressure of the vessel were ramped down to 45°C and 10 MPa in 1 hour, and last, the vessel was slowly depressurized (0.3 ml min^{-1}) to atmosphere for 15 hours using a syringe pump. The resulting freestanding nanoporous graphene inherited the morphological features of bicontinuous np-Ni substrates and was constructed from fully interconnected and covalently bonded graphene sheets in 3D nanoporous nanoarchitecture (Fig. 1, A and C). The unique bicontinuous structure and strong covalent bonding of the nanoporous graphene provided excellent integrity in addition to its properties as a scalable nanoporous material (fig. S9). The densities of the dry and clean nanoporous graphene samples were determined by measuring the weight and dimensions of the bulk nanoporous graphene. The weight was measured by Mettler Toledo Ultra Microbalances with a readability of 0.1 μg, and the thickness of the centimeter-sized samples was measured by SEM.

Microstructure characterization

The morphologies and pore sizes of the nanoporous graphene samples were characterized by SEM (JIB-4600F, JEOL Ltd.) at an operation voltage of 15 kV. The structure of the nanoporous graphene was observed by a HRTEM (JEM-2100F, JEOL Ltd.) equipped with an image aberration corrector. Raman spectroscopy (Renishaw) with an excitation wavelength of 514 nm and a laser power of 5 mW was used to characterize the structure and crystallinity of the nanoporous graphene. The I_D/I_G ratios were used to present the defects in graphene. The shape of the 2D peak, I_{2D}/I_G ratios, and FWHM were used to estimate the layer number of graphene walls in the nanoporous structure. The tube sizes were measured by an ImageJ software package from SEM images. At least two SEM images for each sample were used to evaluate tube sizes. All measured tube sizes were transferred to a histogram chart, and the peak values of the size distributions were used as the average tube sizes (fig. S10). In addition to Raman measurements and TEM characterization, the wall thickness (i.e., number of layer) of graphene, particularly multilayered ones, was also estimated by the specific surface area and density of nanoporous graphene@Ni after CVD growth under different conditions. The specific surface area was determined by the BET method using a high-precision surface area analyzer (BELSORP-mini II, BEL Japan Inc.) at 77.0 K. The wall thickness of graphene was then determined by the density of nanoporous graphene and the specific surface area of the nanoporous structure according to the Supplementary Materials.

Mechanical testing

Mechanical properties of nanoporous graphene were evaluated by tensile and indentation tests. A high-precision Shimadzu EZ-SX instrument equipped with 1 and 500 N load cells was used to perform tensile tests of nanoporous graphene at a strain rate of 8.3×10^{-4} s^{-1}. Tensile samples were cut into a dog bone shape with a gauge length of 6 mm, a width of 2 mm, and a thickness of 35 μm. Indentation experiments were carried out using a nano-/micro-indentation machine (DUH-W201S, Shimadzu) with a 20-μm spherical diamond tip. Nanoporous graphene samples with dimensions of 3 mm by 2 mm and a thickness of ~200 μm were prepared for compression testing. The total indentation depth was kept lower than 20 μm (10% of sample thickness) to avoid constraints from substrates. Hardness and elastic modulus were extracted from loading-unloading curves using the Field-Swain method (*43*).

SUPPLEMENTARY MATERIALS

Supplementary material for this article is available at http://advances.sciencemag.org/cgi/content/full/5/2/eaat6951/DC1

Fig. S1. Raman characterization of nanoporous graphene.
Fig. S2. SEM images of nanoporous graphene with different feature sizes and densities.
Fig. S3. Compression properties of nanoporous graphene.
Fig. S4. Mechanical properties versus density of various high-performance ultralight materials.
Fig. S5. SEM images taken from in situ tensile measurements of nanoporous graphene with a density of 49 mg cm^{-3}.
Fig. S6. SEM images taken from in situ tensile measurements of nanoporous graphene with a density of 11 mg cm^{-3}.
Fig. S7. In situ SEM observations of tensile deformation and failure of nanoporous graphene with a low density of 11 mg cm^{-3}.
Fig. S8. Specific tensile strength versus tensile strain to fracture of nanoporous graphene.
Fig. S9. SEM image and digital photo of nanoporous graphene with a growth temperature of 1000°C and a thickness of 10 μm.
Fig. S10. Tube/pore size distribution of nanoporous graphene under different CVD conditions.
Table S1. Relationship between CVD condition, density, tube size, and tension testing results of nanoporous graphene.
Table S2. Indentation testing results of nanoporous graphene with different densities.

REFERENCES AND NOTES

1. O. A. Tertuliano, J. R. Greer, The nanocomposite nature of bone drives its strength and damage resistance. *Nat. Mater.* **15**, 1195–1202 (2016).
2. R. Lakes, Materials with structural hierarchy. *Nature* **361**, 511–515 (1993).
3. L. R. Meza, S. Das, J. R. Greer, Strong, lightweight, and recoverable three-dimensional ceramic nanolattices. *Science* **345**, 1322–1326 (2014).
4. X. Zheng, W. Smith, J. Jackson, B. Moran, H. Cui, D. Chen, J. Ye, N. Fang, N. Rodriguez, T. H. Weisgraber, C. M. Spadaccini, Multiscale metallic metamaterials. *Nat. Mater.* **15**, 1100–1106 (2016).
5. K. Sun, T.-S. Wei, B. Y. Ahn, J. Y. Seo, S. J. Dillon, J. A. Lewis, 3D printing of interdigitated Li-ion microbattery architectures. *Adv. Mater.* **25**, 4539–4543 (2013).
6. S. Xu, Z. Yan, K.-I. Jang, W. Huang, H. Fu, J. Kim, Z. Wei, M. Flavin, J. McCracken, R. Wang, A. Badea, Y. Liu, D. Xiao, G. Zhou, J. Lee, H. U. Chung, H. Cheng, W. Ren, A. Banks, X. Li, U. Paik, R. G. Nuzzo, Y. Huang, Y. Zhang, J. A. Rogers, Assembly of micro/nanomaterials into complex, three-dimensional architectures by compressive buckling. *Science* **347**, 154–159 (2015).
7. L. J. Gibson, M. F. Ashby, *Cellular Solids: Structure and Properties* (Cambridge Univ. Press, ed. 2, 1999).
8. M. F. Ashby, Y. J. M. Brechet, Designing hybrid materials. *Acta Mater.* **51**, 5801–5821 (2003).
9. X. Zheng, H. Lee, T. H. Weisgraber, M. Shusteff, J. DeOtte, E. B. Duoss, J. D. Kuntz, M. M. Biener, Q. Ge, J. A. Jackson, S. O. Kucheyev, N. X. Fang, C. M. Spadaccini, Ultralight, ultrastiff mechanical metamaterials. *Science* **344**, 1373–1377 (2014).
10. S. C. Han, J. W. Lee, K. Kang, A new type of low density material: Shellular. *Adv. Mater.* **27**, 5506–5511 (2015).
11. Y. Wu, N. Yi, L. Huang, T. Zhang, S. Fang, H. Chang, N. Li, J. Oh, J. A. Lee, M. Kozlov, A. C. Chipara, H. Terrones, P. Xiao, G. Long, Y. Huang, F. Zhang, L. Zhang, X. Lepró, C. Haines, M. D. Lima, N. P. Lopez, L. P. Rajukumar, A. L. Elias, S. Feng, S. J. Kim, N. T. Narayanan, P. M. Ajayan, M. Terrones, A. Aliev, P. Chu, Z. Zhang, R. H. Baughman, Y. Chen, Three-dimensionally bonded spongy graphene material with super compressive elasticity and near-zero Poisson's ratio. *Nat. Commun.* **6**, 6141 (2015).
12. G.-H. Lee, R. C. Cooper, S. J. An, S. Lee, A. van der Zande, N. Petrone, A. G. Hammerberg, C. Lee, B. Crawford, W. Oliver, J. W. Kysar, J. Hone, High strength chemical vapor deposited graphene and grain boundaries. *Science* **340**, 1073–1076 (2013).
13. Z. Chen, W. Ren, L. Gao, B. Liu, S. Pei, H.-M. Cheng, Three-dimensional flexible and conductive interconnected graphene networks grown by chemical vapour deposition. *Nat. Mater.* **10**, 424–428 (2011).

14. M. Mecklenburg, A. Schuchardt, Y. K. Mishra, S. Kaps, R. Adelung, A. Lotnyk, L. Kienle, K. Schulte, Aerographite: Ultra lightweight, flexible nanowall, carbon microtube material with outstanding mechanical performance. *Adv. Mater.* **24**, 3437 (2012).
15. Y. Xu, K. Sheng, C. Li, G. Shi, Self-assembled graphene hydrogel via a one-step hydrothermal process. *ACS Nano* **4**, 4324–4330 (2010).
16. C. Zhu, T. Y.-J. Han, E. B. Duoss, A. M. Golobic, J. D. Kuntz, C. M. Spadaccini, M. A. Worsley, Highly compressible 3D periodic graphene aerogel microlattices. *Nat. Commun.* **6**, 6962 (2015).
17. L. Qiu, J. Z. Liu, S. L. Y. Chang, Y. Wu, D. Li, Biomimetic superelastic graphene-based cellular monoliths. *Nat. Commun.* **3**, 1241 (2012).
18. S. Barg, F. M. Perez, N. Ni, P. do Vale Pereira, R. C. Maher, E. Garcia-Tuñon, S. Eslava, S. Agnoli, C. Mattevi, E. Saiz, Mesoscale assembly of chemically modified graphene into complex cellular networks. *Nat. Commun.* **5**, 4328 (2014).
19. S. Vinod, C. S. Tiwary, P. A. da Silva Autreto, J. Taha-Tijerina, S. Ozden, A. C. Chipara, R. Vajtai, D. S. Galvao, T. N. Narayanan, P. M. Ajayan, Low-density three-dimensional foam using self-reinforced hybrid two-dimensional atomic layers. *Nat. Commun.* **5**, 4541 (2014).
20. X. Xie, Y. Zhou, H. Bi, K. Yin, S. Wan, L. Sun, Large-range control of the microstructures and properties of three-dimensional porous graphene. *Sci. Rep.* **3**, 2117 (2013).
21. H. Sun, Z. Xu, C. Gao, Multifunctional, ultra-flyweight, synergistically assembled carbon aerogels. *Adv. Mater.* **25**, 2554–2560 (2013).
22. Y. Ito, Y. Tanabe, H.-J. Qiu, K. Sugawara, S. Heguri, N. H. Tu, K. K. Huynh, T. Fujita, T. Takahashi, K. Tanigaki, M. W. Chen, High-quality three-dimensional nanoporous graphene. *Angew. Chem. Int. Ed.* **53**, 4822–4826 (2014).
23. Y. Ito, H.-J. Qiu, T. Fujita, Y. Tanabe, K. Tanigaki, M. W. Chen, Bicontinuous nanoporous N-doped graphene for the oxygen reduction reaction. *Adv. Mater.* **26**, 4145–4150 (2014).
24. L. M. Malard, M. A. Pimenta, G. Dresselhaus, M. S. Dresselhaus, Raman spectroscopy in graphene. *Phys. Rep.* **473**, 51–87 (2009).
25. S. S. Chen, W. W. Cai, R. D. Piner, J. W. Suk, Y. P. Wu, Y. J. Ren, J. Y. Kang, R. S. Ruoff, Synthesis and characterization of large-area graphene and graphite films on commercial Cu–Ni alloy foils. *Nano Lett.* **11**, 3519–3525 (2011).
26. X. S. Li, W. W. Cai, J. H. An, S. Kim, J. Nah, D. X. Yang, R. Piner, A. Velamakanni, I. Jung, E. Tutuc, S. K. Banerjee, L. Colombo, R. S. Ruoff, Large-area synthesis of high-quality and uniform graphene films on copper foils. *Science* **324**, 1312–1314 (2009).
27. N.-R. Kang, Y.-C. Kim, H. Jeon, S. K. Kim, J. Jang, H. N. Han, J.-Y. Kim, Wall-thickness-dependent strength of nanotubular ZnO. *Sci. Rep.* **7**, 4327 (2017).
28. M. M. Biener, J. Ye, T. F. Baumann, Y. M. Wang, S. J. Shin, J. Biener, A. V. Hamza, Ultra-strong and low-density nanotubular bulk materials with tunable feature sizes. *Adv. Mater.* **26**, 4808–4813 (2014).
29. T. A. Schaedler, A. J. Jacobsen, A. Torrents, A. E. Sorensen, J. Lian, J. R. Greer, W. B. Carter, Ultralight metallic microlattices. *Science* **334**, 962–965 (2011).
30. N. Ni, S. Barg, E. Garcia-Tuñon, F. M. Perez, M. Miranda, C. Lu, C. Mattevi, E. Saiz, Understanding mechanical response of elastomeric graphene networks. *Sci. Rep.* **5**, 13712 (2015).
31. H. Hu, Z. Zhao, W. Wan, Y. Gogotsi, J. Qiu, Ultralight and highly compressible graphene aerogels. *Adv. Mater.* **25**, 2219–2223 (2013).
32. J. Bauer, A. Schroer, R. Schwaiger, O. Kraft, Approaching theoretical strength in glassy carbon nanolattices. *Nat. Mater.* **15**, 438–444 (2016).
33. H. Bi, I.-W. Chen, T. Lin, F. Huang, A new tubular graphene form of a tetrahedrally connected cellular structure. *Adv. Mater.* **27**, 5943–5949 (2015).
34. M. A. Worsley, S. O. Kucheyev, J. H. Satcher Jr., A. V. Hamza, T. F. Baumann, Mechanically robust and electrically conductive carbon nanotube foams. *Appl. Phys. Lett.* **94**, 073115 (2009).
35. K. H. Kim, Y. S. Oh, M. F. Islam, Mechanical and thermal management characteristics of ultrahigh surface area single-walled carbon nanotube aerogels. *Adv. Funct. Mater.* **23**, 377–383 (2013).
36. L. C. Montemayor, W. H. Wong, Y.-W. Zhang, J. R. Greer, Insensitivity to flaws leads to damage tolerance in brittle architected meta-materials. *Sci. Rep.* **6**, 20570 (2016).
37. A. Nieto, B. Boesl, A. Agarwal, Multi-scale intrinsic deformation mechanisms of 3D graphene foam. *Carbon* **85**, 299–308 (2015).
38. L. R. Meza, A. J. Zelhofer, N. Clarke, A. J. Mateos, D. M. Kochmann, J. R. Greer, Resilient 3D hierarchical architected metamaterials. *Proc. Natl. Acad. Sci. U.S.A.* **112**, 11502–11507 (2015).
39. T. Fujita, L.-H. Qian, K. Inoke, J. Erlebacher, M.-W. Chen, Three-dimensional morphology of nanoporous gold. *Appl. Phys. Lett.* **92**, 251902 (2008).
40. A. P. Robertsa, E. J. Garboczi, Elastic properties of model random three-dimensional open-cell solids. *J. Mech. Phys. Solids* **50**, 33–55 (2002).
41. Y. Tanabe, Y. Ito, K. Sugawara, D. Hojo, M. Koshino, T. Fujita, T. Aida, X. D. Xu, K. K. Huynh, H. Shimotani, T. Adschiri, T. Takahashi, K. Tanigaki, H. Aoki, M. W. Chen, Electric properties of Dirac fermions captured into 3D nanoporous graphene networks. *Adv. Mater.* **28**, 10304–10310 (2016).
42. H.-J. Qiu, J. L. Kang, P. Liu, A. Hirata, T. Fujita, M. W. Chen, Fabrication of large scale nanoporous nickel with a tunable pore size for energy storage. *J. Power Sources* **247**, 896–905 (2014).
43. J. S. Field, M. V. Swain, A simple predictive model for spherical indentation. *J. Mater. Res.* **8**, 297–306 (1993).

Acknowledgments: We thank T. Furuhara at the Institute for Materials Research, Tohoku University, for in situ SEM tensile testing. **Funding:** This work was supported by the Whiting School of Engineering, Johns Hopkins University, and was partially sponsored by JST-CREST "Phase Interface Science for Highly Efficient Energy Utilization," JST, Japan. **Author contributions:** M.C. conceived and supervised this study. H.K. prepared the nanoporous graphene samples and conducted the mechanical measurements and Raman and SEM characterization. H.K., Y.I., and J.H. contributed to the CVD synthesis of nanoporous graphene. P.L. performed TEM characterization. M.C. and H.K. wrote the manuscript. All authors contributed to data analysis and discussion. **Competing interests:** The authors declare that they have no competing interests. **Data and materials availability:** All data needed to evaluate the conclusions in the paper are present in the paper and/or the Supplementary Materials. Additional data related to this paper may be requested from the authors.

Submitted 25 March 2018
Accepted 4 January 2019
Published 15 February 2019
10.1126/sciadv.aat6951

Citation: H. Kashani, Y. Ito, J. Han, P. Liu, M. Chen, Extraordinary tensile strength and ductility of scalable nanoporous graphene. *Sci. Adv.* **5**, eaat6951 (2019).

Extraordinary tensile strength and ductility of scalable nanoporous graphene

Hamzeh Kashani, Yoshikazu Ito, Jiuhui Han, Pan Liu and Mingwei Chen

Sci Adv **5** (2), eaat6951.
DOI: 10.1126/sciadv.aat6951